Sensitivity of horizontal flows to forcing geometry

By ISAO KANDA and P. F. LINDEN

Department of Mechanical and Aerospace Engineering, University of California, San Diego,
La Jolla, CA 92093-0411, USA

We investigate the horizontal flow produced by source–sink forcing in a stably stratified fluid. The forcing jets are kept laminar and are placed along the boundary of a square domain. We find that the resultant flow patterns are extremely sensitive to the forcing geometry. The single dominant vortex pattern, interpreted as the result of inverse energy cascade of two-dimensional turbulence in our previous work (Boubnov, Dalziel & Linden 1994), turns out to be a special case. We show that some of the steady patterns resemble the eigenmodes of the Helmholtz equation as the inviscid vorticity equation. Although there are significant discrepancies in the streamfunction *vs.* vorticity relations between the observed flows and the analytical solutions, we identify the differences as a result of viscous diffusion of vorticity from the source flows. We also study the transition from forced to decaying flow. The flow assumes the properties of Stokes flow at quite large Reynolds number, indicating transformation into patterns with small advective acceleration.

1. Introduction

We investigate the horizontal regime of source–sink forced stratified flow. Horizontal flows produced by source–sink forcing serve as a model of inland seas, the stratosphere, or solar heat exchangers. These flows tend to form organized structures which determine the transport of microorganisms, pullutants, or heat. In this paper, we are mainly concerned with the dependence of the resultant velocity field on the forcing geometry in a square domain. The horizontal flow is produced by the same method as Boubnov, Dalziel & Linden (1994, hereinafter referred to as BDL); the fluid at the same level in a stably stratified salt water is circulated by sources and sinks. BDL used a square tank, fixed the positions of the sources and the sinks, and studied the dependence on the forcing strength. The forcing strength was measured by the Froude number $F = V/Nd$, where N is the buoyancy frequency of the stable stratification, d is the diameter of the source–sink pipes, and V is the fluid velocity at the orifices of the pipes. When $F \lesssim 10$, the induced vortices interacted irregularly for a while, but after sufficient time, they merged into a single vortex. BDL attributed this behaviour to the inverse energy cascade of two-dimensional turbulence. When $F \gtrsim 10$, the kinetic energy of the source flows was so large that mixing occurred and reduced N so that the vertical momentum became comparable to the horizontal momentum and the induced three-dimensional vortices kept interacting. Throughout this paper, the forcing strength is $F \leqslant 5.7$ and the velocity field is horizontal.

Considering the initial random vortex interaction shown in BDL, we expected little dependence on the forcing geometry, and our primary interest was the property of

the developed single vortex, e.g. the robustness against disturbances after it has been established. However, we found that the resultant flow pattern is extremely sensitive to the source–sink forcing geometry. With eight source–sink pairs as in BDL, the resultant flow is either an unsteady irregular or a steady single-vortex pattern. As we reduced the number of source–sink pairs from eight to four to simplify the problem, we found other steady patterns, e.g. four-vortex and five-vortex patterns.

In order to understand the problem, we view it from two perspectives: two-dimensional turbulence and laminar jet interaction. According to two-dimensional turbulence theories, organized flow structure emerges from a random disordered flow with large but finite Reynolds number *Re*. This is true if the flow is two-dimensional down to the Kolmogorov scale and both the fine-scale motion and the forcing are disordered. However, none of these conditions are strictly satisfied in our case. The other viewpoint, laminar jet interaction, focuses on the individual forcing and tries to determine the resultant flow. Since no significant instability is observed, the laminar approximation is plausible. However, laminar jets in a confined geometry are known to exhibit complicated bifurcation behaviour even with one or two jets (Sobey & Drazin 1986; Goodwin & Schowalter 1996). With four or eight source–sink forcing pairs, the complexity is expected to be formidable and we postpone this approach to future work. In this paper, we compare the general solutions to the inviscid two-dimensional flows with observations, and show that some of the observed flow patterns are similar to the large-scale organized structures expected for two-dimensional turbulence.

The organization of this paper is as follows. In §2 we describe the experimental method and show the results of eight-pair and four-pair forcing. In §3 we show that the steady patterns resemble some of the solutions to the steady Euler equation. Among the uncountably infinite solutions, we chose a linear relation between the streamfunction and the vorticity, which is incidentally the same as the result of Chavanis & Sommeria (1996) on two-dimensional turbulence. These solutions are approximately equal to the eigenmodes in a square domain with homogeneous boundary conditions. However, the measured relations between the streamfunction and the vorticity are different from those of the eigenmodes. In §4 we assume that this discrepancy is caused by viscosity, and examine the viscous diffusion in the initial stage of the pattern formation. We will also show the decay behaviour when the forcing is stopped. The smooth transition to the low-*Re* eigenmodes, studied by Konijnenberg, Flór & van Heijst (1998) gives partial support for the assumption that the observed steady patterns are homogeneous eigenmodes modified by viscosity.

2. Flow patterns for various forcing configurations

2.1. *Apparatus*

The apparatus shown in figure 1 is essentially the same as the one used in BDL. The fluid flow is made horizontal by the stable stratification of salt water in a square tank. The inner dimension of the tank is $59.7 \times 59.7 \times 40.6$ cm. Linear stable stratification is established by the double-bucket method. For all the experiments, the buoyancy frequency is $N = 1.5 \, \text{s}^{-1}$. The value of N away from the top and bottom boundaries decreases only 4% after a 10-day experiment. The depth of the fluid is 20 cm and the top surface is free. For flow visualization, Pliolite VT particles (Goodyear chemicals, mean density $\sim 1.022 \, \text{g cm}^{-3}$, size 600–850 $\mu\text{m}\phi$) are seeded in the fluid. About 7 cm below the surface, they form a double layer (about 7 mm layers separated by about 25 mm) due to the characteristic density variation of the particles. The flow is produced

(a)

40.6 cm

(b)

59.7 cm
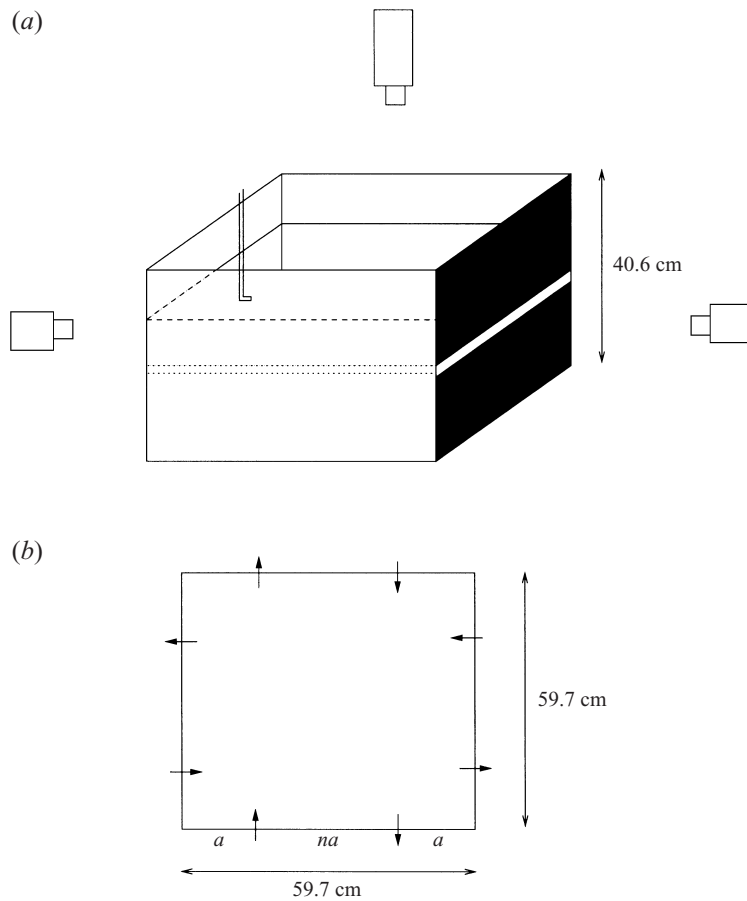
a na a

59.7 cm

FIGURE 1. Apparatus. (a) Overall sketch. Only one forcing pipe is drawn here. (b) Plan view showing the source–sink forcing configuration. The pipe intervals *a-na-a* will be used to represent the configurations of four-pair experiments.

in the middle of this double layer where the seeding density is low by four or eight source–sink pairs along the walls. The sources and sinks are made of 1/8 in. inner diameter pipes bent at a right angle near the orifices so that the introduced flow is horizontal. They are connected to individual channels of a peristaltic pump and fluid of the same density is sucked into the sinks and re-introduced from the sources. The variation of the flow rates between channels is at most 5%.

The peristaltic pump works by squeezing the transfer tubes by a cyclic motion of rollers and create a pulsating motion with the pulse amplitude comparable to the mean flow rate. Since the pulsation frequency is larger than N or the inverse of the time scale of the observed motion, it has negligible effect on the resultant flow. In BDL, the Reynolds number was defined as $Re = Vd/\nu$ where V is calculated from the temporal mean volume flow rate, d is the inner diameter of the pipes, and ν is the kinematic viscosity of the fluid. Although Re in BDL and in this article is $O(10^2)$, the effective Re is considerably larger at the maximum velocity in the pulse. Hence the source and the sink flows have the following properties. At the source orifice, a puff of fluid is ejected at the maximum velocity and forms a vortex ring. The ring is pushed straight forward because the source flow retains the cylindrical shape
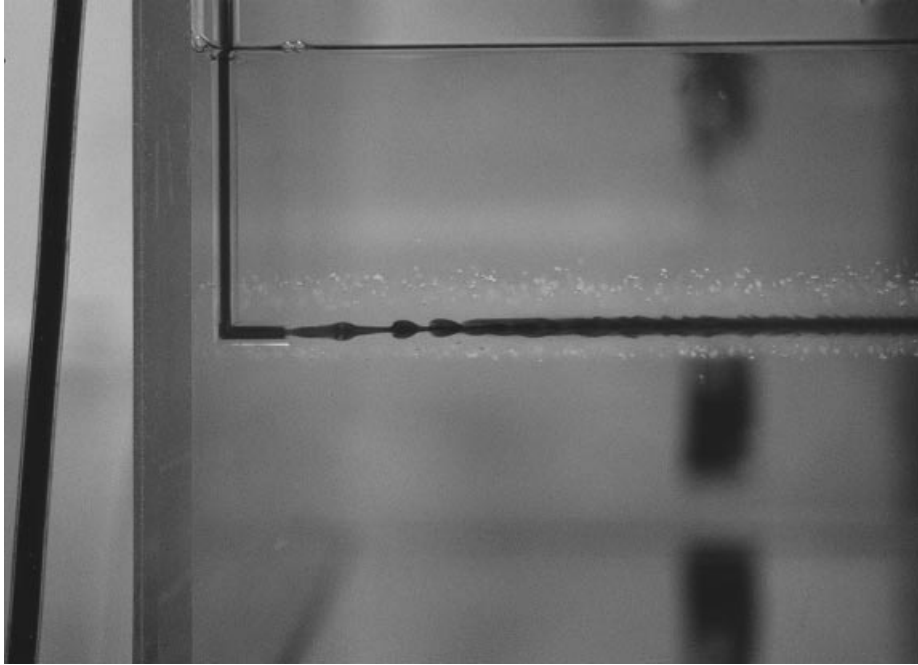
FIGURE 2. Dyed image of the source flow. The conditions are $N = 1.5\,\mathrm{s}^{-1}$, $V = 2.3\,\mathrm{cm\,s}^{-1}$. The seeding particles and their relation to the forcing level may be seen.

due to the vorticity gained inside the pipe. By the induced velocity field, the vortex ring of the next pulse catches up with the one ahead. The successive collision of vortex rings may lead to a turbulent flow, but if the Froude number is sufficiently small, the vertical motion is suppressed and a laminar horizontal flow results. However, small-scale vertical motions are admitted in a layer of thickness comparable to the pipe inner diameter. A dye image is shown in figure 2 for $V = 2.3\,\mathrm{cm\,s}^{-1}$. The source flow is not much different for other values of V. The sink flow is quite different since the velocity profile across the orifice diameter is almost flat. Without significant vorticity, the sink flow is virtually a potential flow and the momentum is distributed in much wider angles than the source flow. As will be shown by the streak images in the following subsections, the source flow appears as a narrow jet and the sink flow is hard to recognize.

The source–sink pairs are positioned in configurations such that they do not impart any significant net thrust or angular momentum. The seeded particles are illuminated by slide projectors from two facing sides. The light goes through slits of about 5 mm. To avoid the shadow cast by the pipes, the slits are about 5 mm below the source–sink pipe orifice level and the lower part of the Pliolite double layer is illuminated, but the flow field at the illuminated level is almost the same as that at the forced level. The plan view of the particle motion is recorded by a CCD camera from above and the velocity field is analysed by DigImage, a particle tracking system developed at DAMTP, Cambridge (Dalziel 1993).

2.2. *Eight-pair forcing*

We first present the case of eight-pair forcing as in BDL which motivated this problem. We find that the interpretation of the formation of a single dominant vortex as the
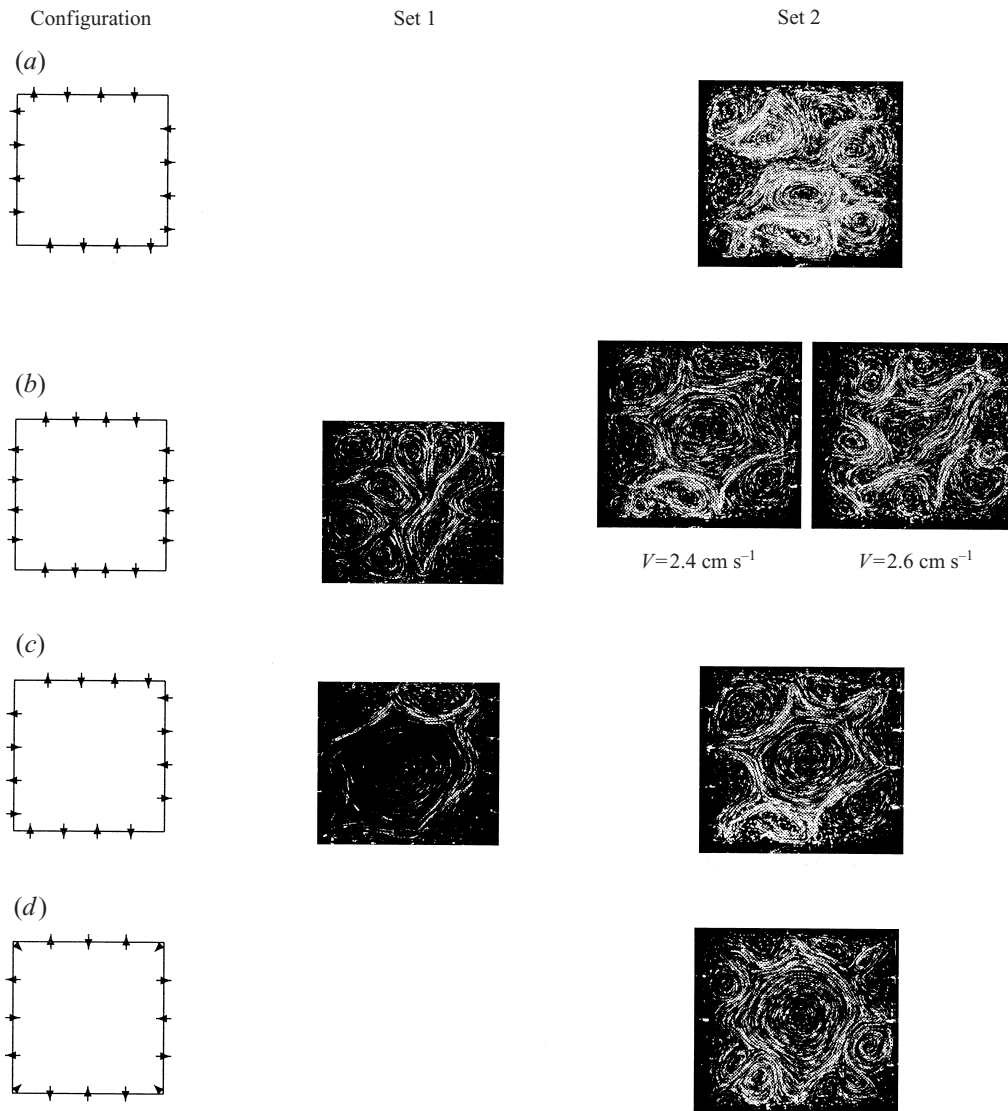
Configuration	Set 1	Set 2

(*a*)

(*b*)

V=2.4 cm s^{-1} V=2.6 cm s^{-1}

(*c*)

(*d*)

FIGURE 3. Source–sink configurations and streak images of two sets of eight-pair forcing experiments. (*a*) BDL type, (*b*) equi-spaced, (*c*) opposite shift to BDL, (*d*) sources at the corners and at the mid-points of the sides.

result of inverse energy cascade is faulty, and the resultant flow is highly affected by the forcing geometry. Four source–sink configurations shown in figure 3 are tested. For all the configurations, no significant net thrust or angular momentum is imparted by the forcing. The configuration (*a*) has source–sink arrays on the sidewalls shifted toward two corners so that sinks at the ends of arrays are closer to the corners than the sources. This configuration is geometrically identical to the one used in BDL. The configuration (*b*) has sources and sinks at equal intervals on the sides and the configuration (*c*) is like (*a*) but shifted in the opposite direction. The configuration (*d*) is different from others and has sources at the corners and the mid-points of the sides. Two sets of experiments are carried out: (*b*) and (*c*) in set 1, and all the configurations

(*a*)   (*b*)

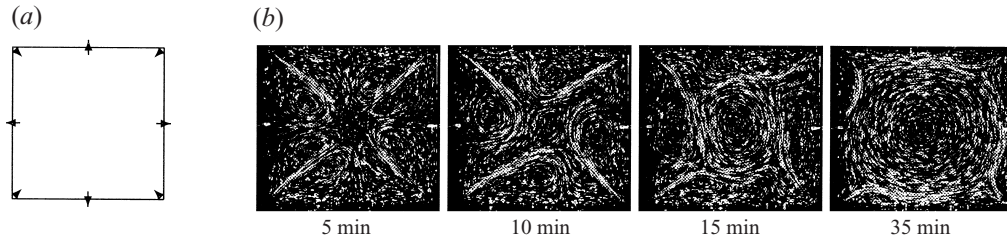5 min   10 min   15 min   35 min

FIGURE 4. (*a*) The corner-source configuration of the four-pair forcing experiment. (*b*) Evolution into the steady single-vortex pattern with $V = 2.3 \, \text{cm s}^{-1}$.

in set 2. The mean velocity at the orifice is $V = 2.4 \, \text{cm s}^{-1}$ except for one of the results of set 2, (*b*), for which $V = 2.6 \, \text{cm s}^{-1}$. The Froude number is $F = 5.0$ or 5.5, well within the regime where BDL observed the formation of a single-vortex pattern.

In set 1, we initially expected the same single-vortex pattern as a result of an inverse energy cascade for any configuration which does not impart any significant net thrust or angular momentum. However, with the configuration (*b*), the velocity field continued to change irregularly without increase in the vortex size. With the configuration (*c*), though we did not observe the initial development, the single-vortex pattern formed within 2 hours. The sparse streaks are due to the poor lighting.

In set 2, the results of set 1 were not exactly reproduced. Both configurations (*c*) and (*b*) resulted in the single-vortex pattern. However, the central vortex with the configuration (*b*) fluctuates more than with the configuration (*c*). The fluctuation is enhanced by increasing V from 2.4 to $2.6 \, \text{cm s}^{-1}$. Though neither of them is strictly steady, we call a flow pattern with small fluctuation, such as the one with $V = 2.4 \, \text{cm s}^{-1}$, a steady pattern. This convention is used throughout this paper. The BDL configuration (*a*) resulted in an unsteady irregular pattern and we could not reproduce their result. The difference in the source positions between (*a*) and (*b*) is 17 mm, only 3% of the side length. Hence the inverse cascade scenario, which should not be affected by the forcing geometry, does not apply to this flow.

Rather than identifying the cause of poor reproducibility, we interpret the results by considering a threshold which is sensitive to small experimental errors. The threshold is defined by the positions of the sources next to the lower-left and the upper-right corners. If these sources are closer to the corners than the threshold positions, a single-vortex pattern appears. Otherwise, the flow changes irregularly. In BDL, the threshold source position may have been to the right of their configuration, while in our first set it is between (*b*) and (*c*), and in our second set it is between (*a*) and (*b*) but very close to (*b*). The plausibility of this interpretation is to be confirmed in the four-pair forcing experiments in the next subsection.

2.3. *Four-pair forcing*

In order to simplify the problem, we reduce the number of source–sink pairs from eight to four. Several configurations are tested and the dependence on the forcing strength is also examined.

When the sources are at the corners and directed toward the domain centre (figure 4*a*), a large vortex occupies most of the domain. This pattern was confirmed to form for $V = 1.7$, 2.3, $3.1 \, \text{cm s}^{-1}$ and, although the velocity of the large vortex changes, its shape is independent of the source strength. The initial evolution is shown in figure 4(*b*). The source flows meet at the centre and then they deflect each other to form a
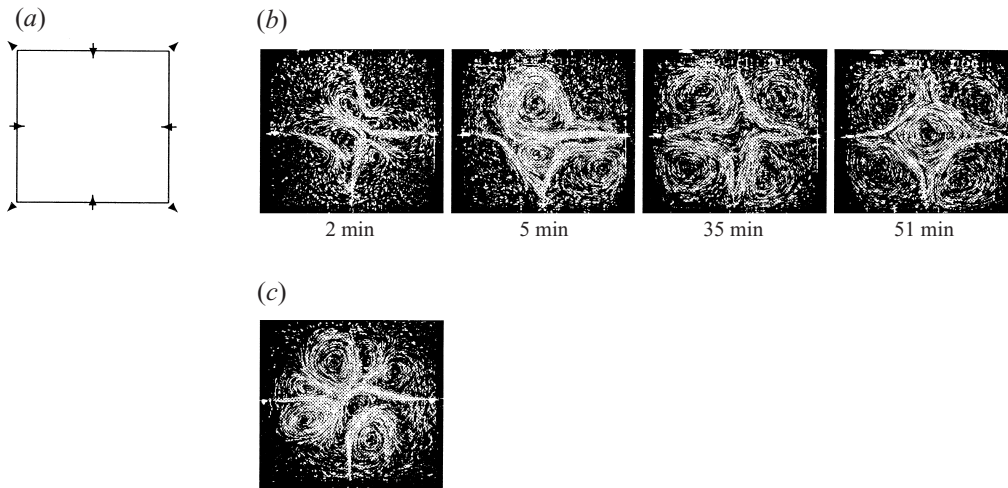
(a)

(b)

2 min   5 min   35 min   51 min

(c)

FIGURE 5. (*a*) The side-source configuration of the four-pair forcing experiment. (*b*) Evolution into the steady five-vortex pattern ($V = 2.3\,\mathrm{cm\,s^{-1}}$) which occurs in one in five trials. (*c*) Unsteady pattern which continues to change irregularly even after leaving overnight.

central vortex. This vortex grows until it occupies the whole domain. Typically, this process takes about 20 min.

When the sources are at the mid-points of the sides (figure 5*a*), a five-vortex pattern forms with about 20% probability (5 out of 25 trials). The major component of this pattern is the central vortex and the four peripheral vortices (the last image of figure 5*b*). The central vortex looks like a square pivoted at the source flows which extend to the square vertices. Most of the momentum is confined in this path connecting the sources and the central vortex. When this steady pattern appears, it does so within an hour. However, the formation is not as straightforward as with the corner-source configuration. As shown in figure 5(*b*), the flow field initially changes irregularly. It comes close to the five-vortex pattern a couple of times and one out of five times it stays steady. Otherwise, large irregular fluctuation about the five-vortex pattern continues (figure 5*c*). The extreme sensitivity of this pattern is exhibited well by the fact that we could not retrieve the steady pattern just by turning off and on the forcing.

To obtain similar configurations to BDL, we put the sources and the sinks at symmetric positions about the mid-points of the sidewalls. We label the configurations by the interval ratios of pipes along a sidewall (see figure 1*b*). For example, when a source and a sink are placed at equal intervals, we call it the *a-a-a* configuration. The symbol *a* is also used for the distance between a corner and the source closest to the corner. The distance between sources and sinks is systematically changed and the dependence on the forcing strength is examined for $V = 1.9, 2.3, 2.7\,\mathrm{cm\,s^{-1}}$.

The flow pattern regimes for three sets of experiments are shown in figure 6. The three sets were done on different occasions and the differences in the results reflect small errors of the set-up. The flow patterns are classified according to the symmetry property and the steadiness. The correspondence between the flow patterns and the figurative signs in figure 6 is explained in figure 7. The time evolution into these patterns is straightforward except for the four-vortex pattern of set 2 which took 2.5 hours to stabilize. The symmetry of the flow pattern can be classified roughly into three types: (i) diagonal ellipse pivoted at the impinging points of the two neighbouring
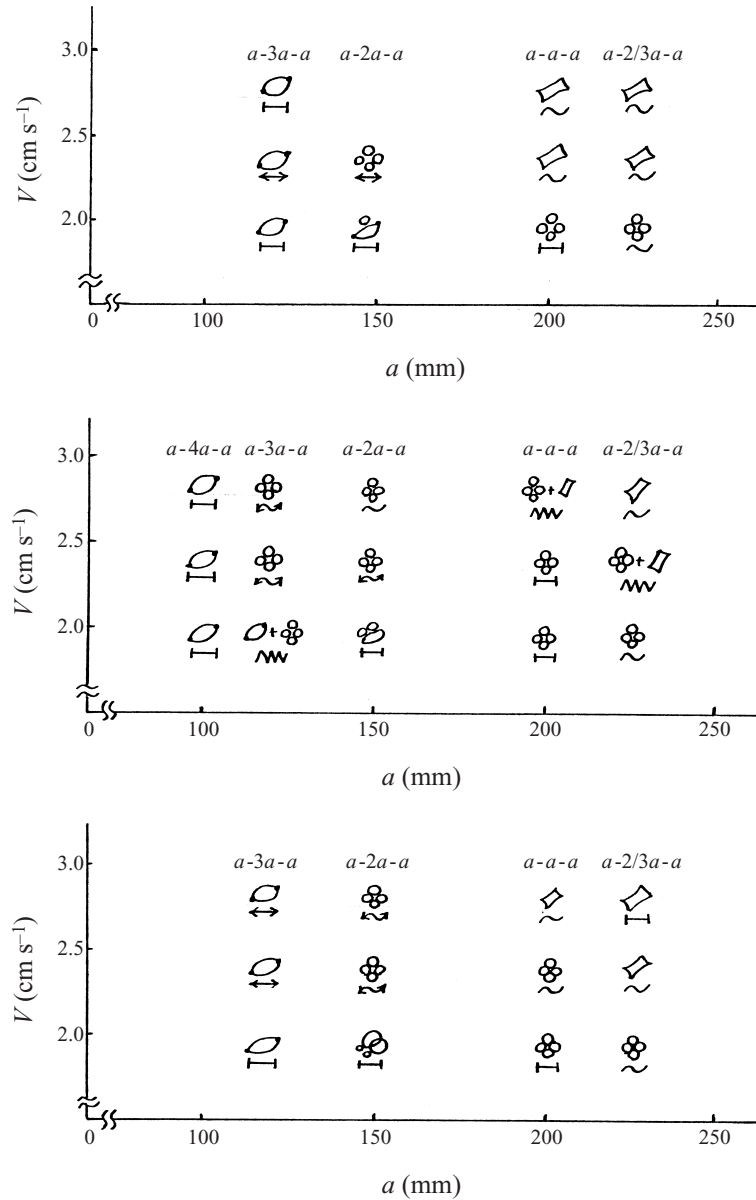
FIGURE 6. Flow pattern regimes for three sets of four-pair forcing experiments. The explanation of the figurative signs is given in figure 7.

sources (*a–c*), (ii) four-vortex pattern (*d–h*), (iii) diagonal rectangle pivoted at the four sources (*i, j*). As the length *a* increases and the flow rate *V* increases, the pattern changes from (i) to (ii) and then to (iii). Near the transitions, the flow pattern loses steadiness and fluctuates irregularly between the patterns. Regular oscillation as shown in figure 7(*g*) can be found depending on the setup condition. As is clearly seen in the three sets, the transition point between the patterns changes significantly between experiments. This is due to the small errors in the experimental setup as we have shown with the eight-pair case. Since the overall dependence on the forcing

geometry is clear and there are many causes of error, such as the flow rate variation, source orifice position and direction, and the source flow pulsation, we did not try to reduce the experimental errors at this stage.

3. Inviscid two-dimensional analysis

In this section, we assume that the flow can be described as a two-dimensional inviscid flow and compare the analytical solutions with observations. We deal only with steady flows. First, we justify the assumption that steady flows can be approximated as two-dimensional and inviscid. Since the observed flow is horizontal, the velocity field may be represented by a streamfunction Ψ of the form

$$\Psi(x, y, z) = \hat{\psi}(z)\psi(x, y), \tag{3.1}$$

where $\hat{\psi}(z)$ is a non-dimensional function with $0 \leqslant \hat{\psi}(z) \leqslant 1$. Then the vertical vorticity ω is

$$\omega = -\hat{\psi}\nabla_H^2\psi, \tag{3.2}$$

where $\nabla_H^2 = \partial^2/\partial x^2 + \partial^2/\partial y^2$. We substitute (3.2) into the vertical component of the vorticity equation

$$(\boldsymbol{u} \cdot \nabla)\omega = \nu\nabla^2\omega. \tag{3.3}$$

Then we obtain

$$\hat{\psi}J(\nabla_H^2\psi, \psi) = \nu\left(\nabla_H^2\nabla_H^2\psi + \frac{1}{\hat{\psi}}\frac{\partial^2\hat{\psi}}{\partial z^2}\nabla_H^2\psi\right), \tag{3.4}$$

where J is the Jacobian. In order to evaluate the magnitude of each term, we need the horizontal and the vertical length scales. From the observed steady motion, the horizontal length scale is the vortex radius, i.e. 100–300 mm. The vertical velocity profile is determined by the viscous diffusion and the top and the bottom boundaries. Hence the vertical length scale is about half the total fluid depth, i.e. 100 mm. Although there is vertical asymmetry in that the top boundary is shear-free and the bottom boundary is non-slip, the point here is that the vertical and the horizontal scales are of the same order. If we consider the region where $\hat{\psi}$ is $O(1)$, the two terms on the right-hand side are comparable. As we will show later, the typical velocity of the steady pattern is $2\,\mathrm{mm\,s^{-1}}$. Using the kinematic viscosity of water $\nu = 10^{-6}\,\mathrm{m^2\,s^{-1}}$, the ratio of the right-hand side to the left-hand side is about 0.0025. Neglecting the right-hand side, the vorticity equation is reduced to

$$J(\nabla_H^2\psi, \psi) = 0, \tag{3.5}$$

which is the two-dimensional steady Euler equation. For simplicity, we will drop the subscript H hereinafter.
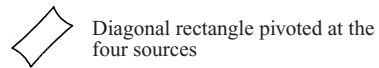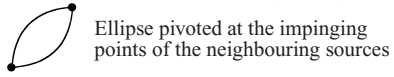
We will consider the BDL type source–sink configurations: symmetrical about one of the diagonals. Other configurations tested in the previous section are included as higher symmetry cases. We employ the Cartesian coordinates with x and y parallel to the sidewalls and the origin at the centre of the domain; x and y are scaled by the sidewall length L, and ψ by LU where U is the typical velocity magnitude. Then, if the boundary condition on $y = -1/2$ is given by
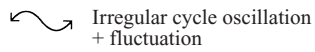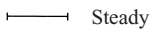
$$\psi(x, -\tfrac{1}{2}) = f(x), \tag{3.6}$$

the other boundary conditions are

$$\psi(x, \tfrac{1}{2}) = f(-x), \quad \psi(-\tfrac{1}{2}, y) = -f(y), \quad \psi(\tfrac{1}{2}, y) = -f(-y). \tag{3.7}$$

428   *I. Kanda and P. F. Linden*

- Symmetry classes

Ellipse pivoted at the impinging points of the neighbouring sources

Deformed pivoted ellipse

Four-vortex pattern

Deformed four-vortex pattern

Deformed four-vortex pattern

Diagonal rectangle pivoted at the four sources

- Steadiness classes

⊢——⊣ Steady

⌢ Fluctuation

⟵⟶ Regular cycle clean oscillation

Irregular cycle oscillation + fluctuation

∧∧∧ Irregular unsteady

- Examples of streak images

(a)

(b)

(c)

(d)

(e)

(f)
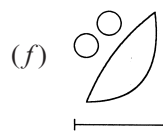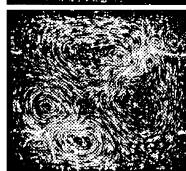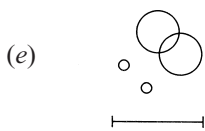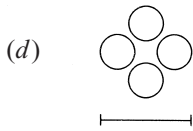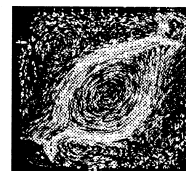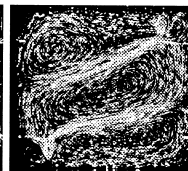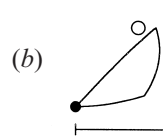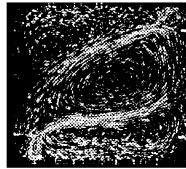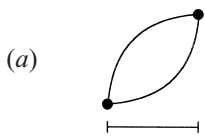
FIGURE 7 (*a–f*). For caption see facing page.

FIGURE 7. Explanation of the figurative signs in figure 6.

The boundary function $f(x)$ represents the source–sink mass flux through the forcing pipes. Since the solution must reflect the symmetry of the boundary condition, it satisfies the following relations:
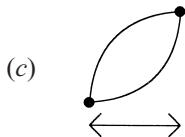
$$\psi(x, y) = \psi(-x, -y)$$
$$= -\psi(y, x). \tag{3.8}$$

The equation $J(\nabla^2\psi, \psi) = 0$ is satisfied if $\nabla^2\psi = h(\psi)$ for an arbitrary continuous

(*a*) $\lambda=2\pi^2$, $\cos\pi x\cos\pi y$
Similar to the single-vortex pattern

(*b*) $\lambda=8\pi^2$, $\sin 2\pi x\sin 2\pi y$

(*c*) $\lambda=10\pi^2$, $\cos\pi x\cos 3\pi y$

(*d*) $\lambda=10\pi^2$, $\cos\pi x\cos 3\pi y-\cos\pi y\cos 3\pi x$
Similar to the four-vortex pattern

(*e*) $\lambda=10\pi^2$, $\cos\pi x\cos 3\pi y+\cos\pi y\cos 3\pi x$
Similar to the five-vortex pattern

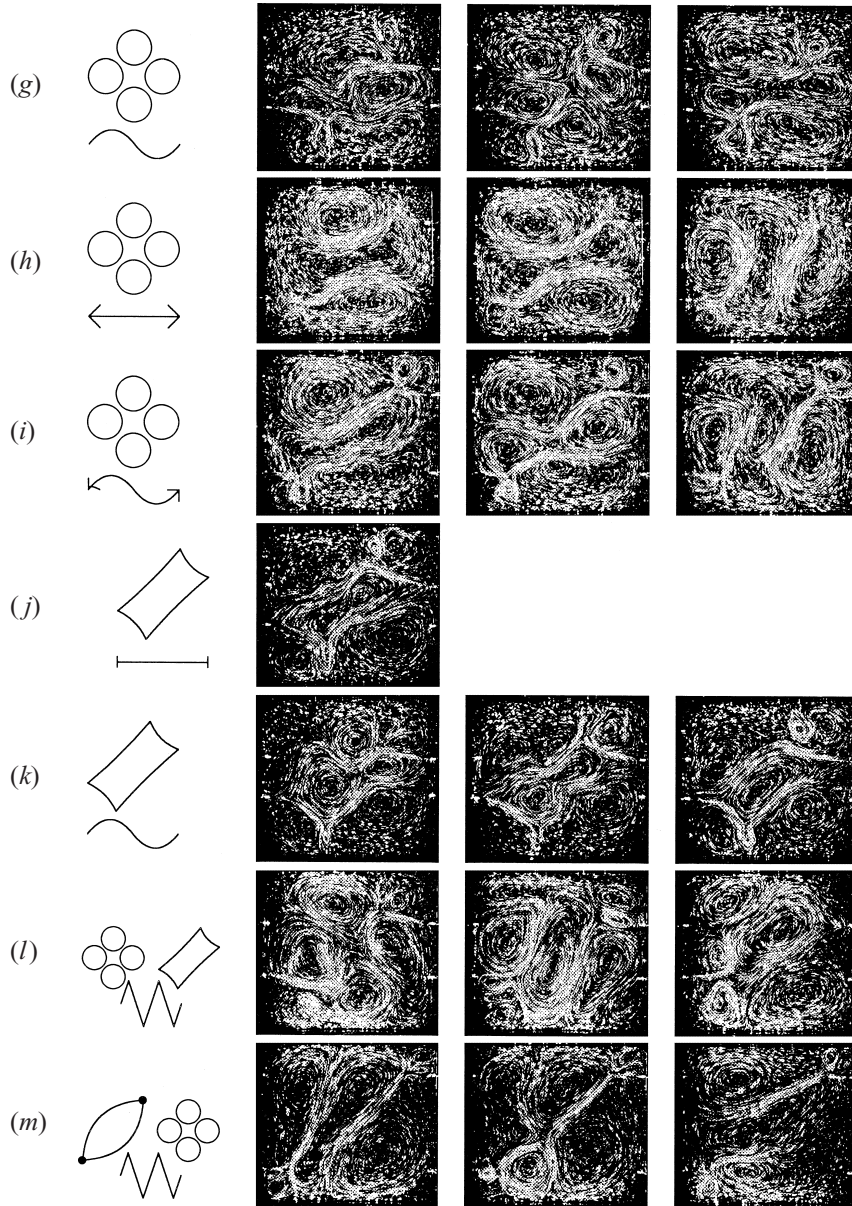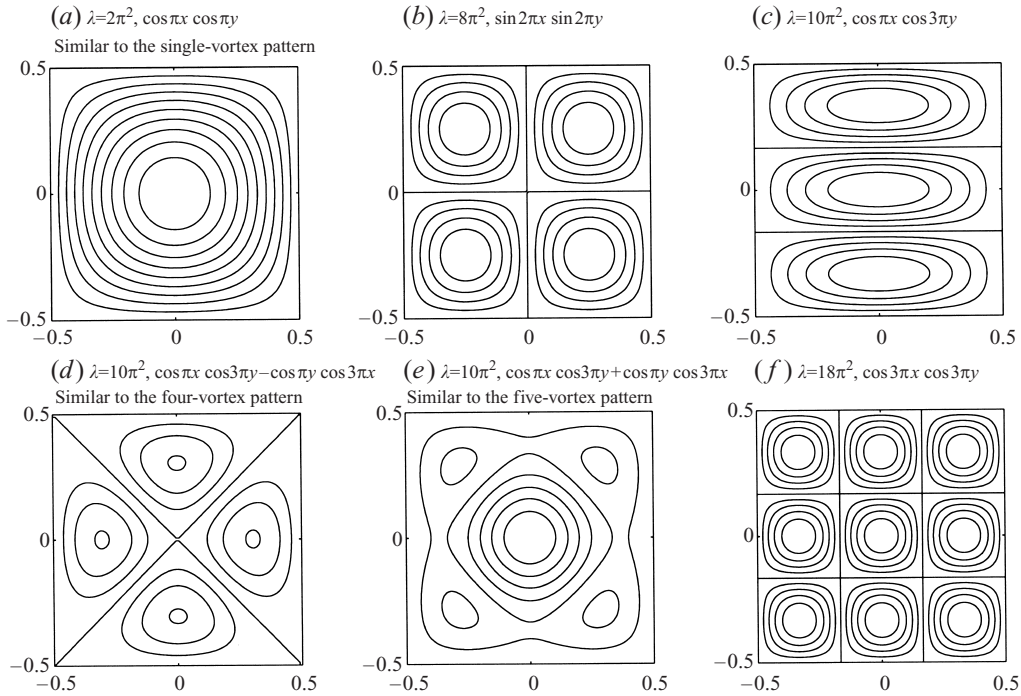(*f*) $\lambda=18\pi^2$, $\cos 3\pi x\cos 3\pi y$

FIGURE 8. Some of the inviscid homogeneous eigenmodes. The real solutions are approximated with these eigenmodes. The eigenmodes (*a*, *d*, *e*) are similar to the observed steady flow patterns.

function $h(\psi)$. We assume a linear relation,

$$h(\psi) = -\lambda^2\psi,$$

i.e.

$$\omega = \lambda^2\psi. \tag{3.9}$$

Although this assumption cannot be justified, it is equivalent to considering the maximum-entropy state of a two-dimensional turbulent flow (Chavanis & Sommeria 1996). If the resultant flow obeys the symmetry of (3.8) completely, we will not obtain solutions like the single-vortex or the five-vortex patterns. In order to accommodate symmetry-breaking solutions, we allow small deviations from the boundary condition (3.6), (3.7) and separate the solutions into two parts: ψ_0 and ψ_1. The first part ψ_0 satisfies $\nabla^2\psi_0 = -\lambda_0^2\psi_0$ with the boundary condition (3.6), (3.7), and the second part ψ_1 satisfies $\nabla^2\psi_1 = -\lambda_1^2\psi_1$ with the boundary condition representing the deviation from (3.6), (3.7). If $\lambda_1^2 = \lambda_0^2$ $(= \lambda^2)$, the simple addition $\psi = \psi_0 + \psi_1$ satisfies $J(\nabla^2\psi, \psi) = 0$ with the boundary condition including the deviations from perfect symmetry. As λ^2 approaches an eigenvalue of the Helmholtz equation for a homogeneous boundary condition ($f \equiv 0$ in (3.6)), the solution ψ becomes dominated by the corresponding eigenmode.

Some of the solutions ψ for the common eigenvalues $\lambda^2 = \lambda_1^2 = \lambda_0^2$ are shown in figure 8. We see the similarity between the solutions and the observed flow patterns as indicated in the figure. The solution (*a*) corresponds to the single-vortex pattern of the corner-source configuration (figure 4*b*), the solution (*d*) to the four-vortex pattern of the *a-a-a* configuration (figure 7*d*), and the solution (*e*) to the five-vortex pattern of the side-source configuration (figure 5*b*).

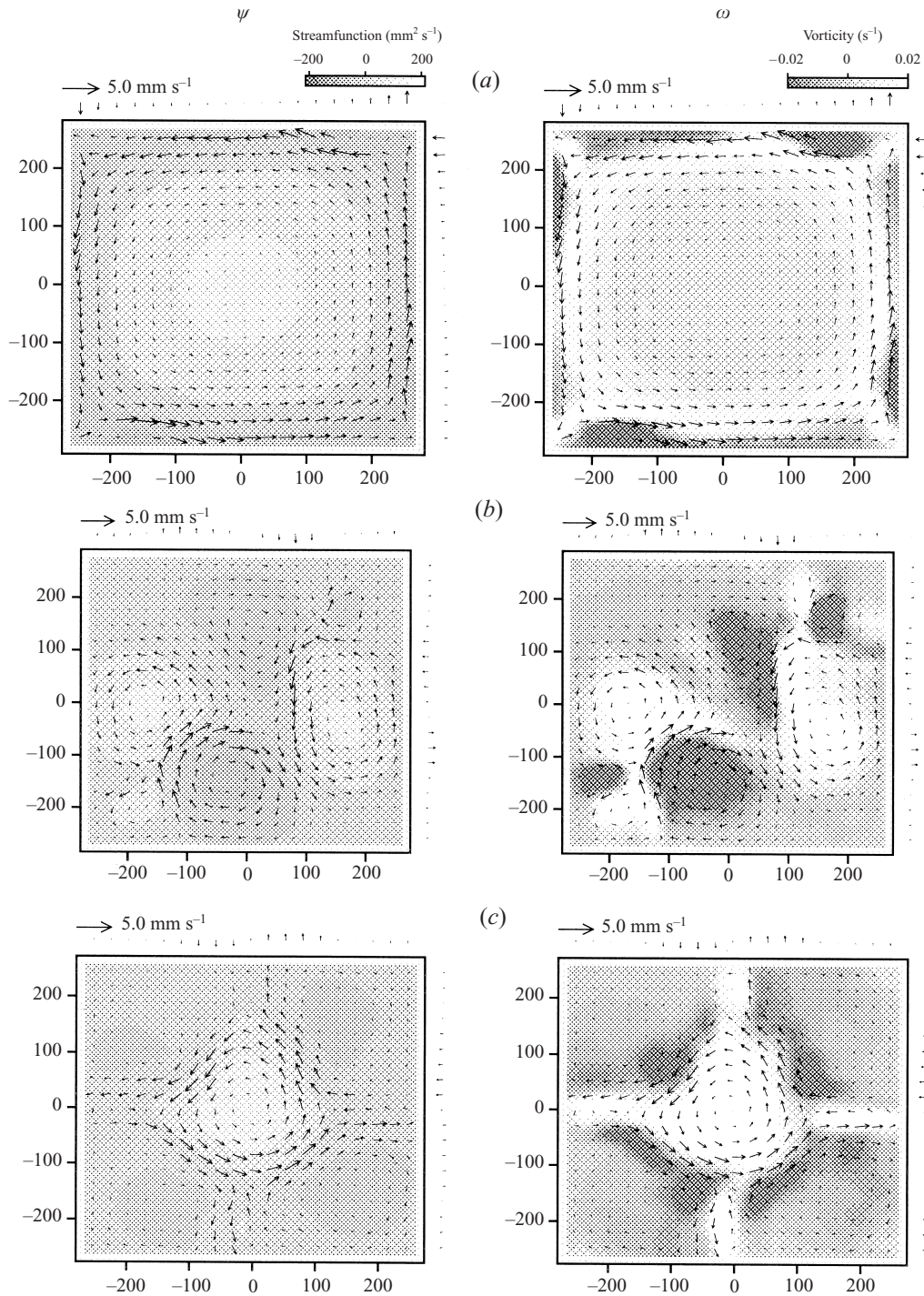FIGURE 9. The contour maps of streamfunction ψ and vorticity ω for three steady patterns: (*a*) the single-vortex pattern by the corner-source configuration with $V = 2.3\,\mathrm{cm\,s^{-1}}$, (*b*) the four-vortex pattern by the *a-a-a* configuration with $V = 1.9\,\mathrm{cm\,s^{-1}}$, (*c*) the five-vortex pattern by the side-source configuration with $V = 2.1\,\mathrm{cm\,s^{-1}}$.
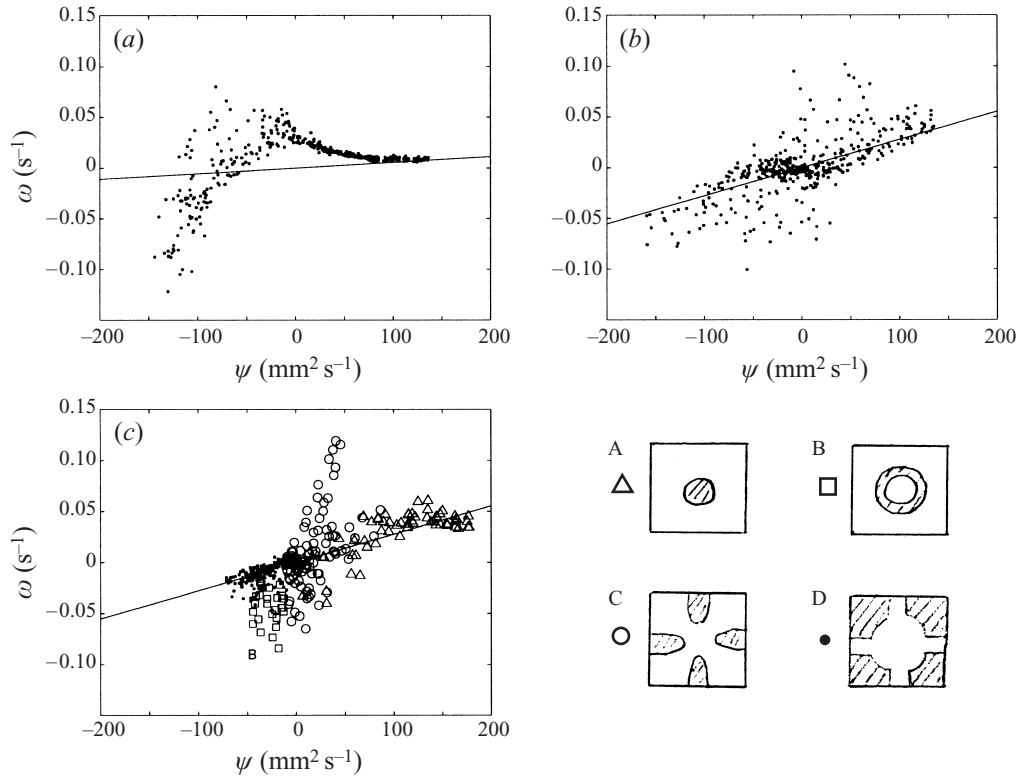
FIGURE 10. ψ–ω relations for the three steady patterns; (a–c) correspond to the same conditions as figure 9. The four regions A–D in (c) correspond to the sketches beside the figure.

When λ^2 is close to $2\pi^2$, ψ_0 tends to zero but the dominant term of ψ_1, i.e. $\cos \pi x \cos \pi y$ has a large amplitude. When λ^2 is close to $10\pi^2$, either $\psi_0 \sim \cos 3\pi x \cos \pi y - \cos \pi x \cos 3\pi y$ or a linear combination of the dominant terms of ψ_1, i.e. $\cos 3\pi x \cos \pi y$ and $\cos \pi x \cos 3\pi y$ have a large amplitude. The form $\cos 3\pi x \cos \pi y + \cos \pi x \cos 3\pi y$ is just one possibility.

Now we compare these possible solutions with the observations more closely. The velocity field obtained by the particle tracking function of DigImage and the contour maps of ψ and ω are shown in figure 9 and ψ–ω relations are shown in figure 10 for the three steady patterns which have similar shapes to the eigensolutions (figure 8a, d, e). The arbitrary constant of the streamfunction is chosen such that the mean value is zero. The lines in figure 10 are the linear relations (3.9) of the analytical solutions with similar spatial structures. For the single-vortex pattern (figure 10a), the discrepancy is obvious. The magnitude of ω near the centre of the vortex (maximum ψ) is close to the line $\omega = 2\pi^2\psi$, but it deviates from the line with a negative slope. The large positive slope in $-150 < \psi < 0$ is due to the source flows along the sidewalls. For the four-vortex pattern (figure 10b), the data points lie parallel to the line $\omega = 10\pi^2\psi$, but with considerable scatter. This is considered to be due to the asymmetry of the pattern as seen in the vorticity contour (figure 9b). For the five-vortex pattern (figure 10c), there are distinctly different regions. The correspondence between the ψ–ω plot and the regions in the flow field is shown beside the plot. The regions B, C, D have overlapping ψ–ω regions, and the division in the ψ–ω plot should be regarded as a coarse one. In the central vortex region A, the relation exhibits a similar character to

the single-vortex pattern: negative slope toward the centre. In the peripheral region B of the central vortex, the vorticity is distributed in a wide negative range for a relatively small range of ψ. This distribution represents a large spatial fluctuation of vorticity in this region where the source flows are contained in a narrow path. In the narrow elongated region C, the ψ–ω relation has a much steeper slope than other regions. The only region in which the ψ–ω relation lies close to the line $\omega = 10\pi^2\psi$ is the region D of the outer four vortices.

From the above analysis, we speculate that the discrepancy is caused by the source flows. Their effect is pronounced when they form enclosed regions as with the single-vortex pattern and the region A of the five-vortex pattern. In an ideal case where the Reynolds number tends to infinity and there is no flux into or out of the domain, the Prandtl–Batchelor theorem predicts a uniform vorticity field as time tends to infinity. A typical application of this theorem is a cavity flow driven by a shearing motion at the cavity opening. The flows associated with the single vortex and region A of the five-vortex pattern deflect the source flows to be tangential to their outer boundaries so the net flux into the region is zero, and we may consider the enclosed regions as isolated. The Reynolds number is too small ($O(10^2)$) for the Prandtl–Batchelor theorem to be valid, but we expect that the vorticity field is affected by the viscous diffusion from the source flows. Hence the negative slope of the ψ–ω relation can be interpreted as a diffusion profile from the large vorticity of the source flows to some constant near the centre. The vorticity diffusion behaviour will be examined in the next section.

4. Effect of viscosity

As we have seen in the previous sections, the effect of viscosity is not negligible. We will examine two aspects of the effect: (i) initial vorticity diffusion, (ii) decay behaviour.

4.1. *Initial vorticity diffusion*

As noted in § 3, vorticity diffusion from the source flows is expected to be responsible for the discrepancy of the ψ–ω relations of the steady patterns from those of the steady inviscid two-dimensional eigenmodes. Here we make use of the measurements of the single-vortex pattern above the forcing level to examine the initial diffusion behaviour. We expect that, at least initially, the flow above the forcing level is similar to a weakly forced case and the region away from the boundary walls is less affected by the source flows. An alternative method would be to use a weak forcing and measure the initial evolution at the forcing level, but then it takes longer to establish the single-vortex pattern and the initial diffusion behaviour is easily missed.

With $V = 2.3\,\mathrm{cm\,s^{-1}}$, the single-vortex pattern established after 20 min, and the evolutions of the ψ–ω relation at the forcing level and at 4.3 cm above the forcing level are shown in figure 11. We can recognize the vorticity diffusion from the source flows to the domain centre. After 20 min, two-thirds of the positive-ψ part is close to the line $\omega = 2\pi^2\psi$ line with a positive slope, but after 240 min, less than half of the positive-ψ part is close to the line and the slope is negative. The diffusion behaviour is much clearer above the forcing level as can be seen in figure 11(b). After 20 min, the positive-ψ data are parallel to $\omega = 2\pi^2\psi$. The origin is shifted because $\psi = 0$ is defined as the mean value in the analysed region, which is smaller than the whole domain. As time progresses, the slope turns negative and most of the positive-ψ part deviates from the line.
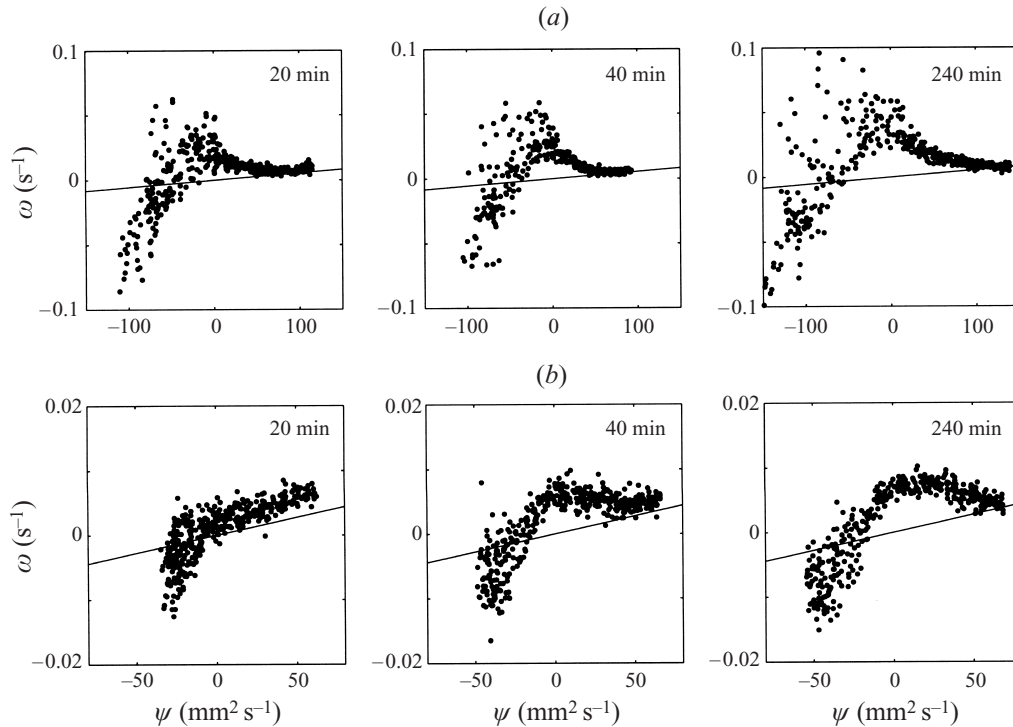
(*a*)

(*b*)

FIGURE 11. Evolution of ψ–ω relations of the single-vortex pattern by the corner-source configuration with $V = 2.3\,\mathrm{cm\,s^{-1}}$ at two different heights: (*a*) at the forcing level and (*b*) at 4.3 cm above the forcing level.

From the above results, we can interpret the single-vortex pattern as an eigenmode of the Helmholtz equation modified by the vorticity diffusion from the source flows. The same is probably true for the four- and the five-vortex pattern. However, for the four-vortex pattern, the establishment time is longer since the flow rate has to be set at $V = 1.9\,\mathrm{cm\,s^{-1}}$, and also the vorticity diffusion is completed much earlier because the vortex radius is half of the single-vortex pattern. For the five-vortex pattern, in addition to the early completion of diffusion, we need to find a straightforward evolution into it. Therefore, it is very difficult to measure the initial diffusion behaviour for these patterns.

4.2. *Decay behaviour*

We showed that the source flows alter the vorticity distribution of the steady patterns but the appearance of the velocity field is almost unchanged. In order to see how much the flow field is altered as the relative magnitude of the viscous force increases, we investigate the decay behaviour after the forcing is stopped. The decaying flow was studied by Konijnenberg, Flór & van Heijst (1998) in relation to two-dimensional turbulence. We briefly recapitulate their calculation with our notations in § 3.

We start with the dimensional vorticity equation,

$$\frac{\partial \omega_*}{\partial t_*} + (\boldsymbol{u}_* \cdot \nabla_*)\omega_* = \nu \nabla_*^2 \omega_*. \tag{4.1}$$

There are two cases where the second term on the left-hand side is negligible compared to the others. The first case is when $Re = UL/\nu \ll 1$ and the decay time scale

is ReL/U. Then by introducing non-dimensional variables: $t_* = (ReL/U)t, x_* = Lx, \omega_* = (U/L)\omega$, we obtain

$$\frac{\partial \omega}{\partial t} = \nabla^2 \omega. \tag{4.2}$$

This case is valid for any type of flow. The second case happens for particular flows for which $|\partial \omega_*/\partial t_*|, v|\nabla_*^2 \omega_*| \gg |(\boldsymbol{u}_* \cdot \boldsymbol{\nabla}_*)\omega_*|$ irrespective of the magnitude of *Re*. This is possible if the flow is a pure shear flow, e.g. a parallel shear flow or a circular shear flow, as long as no instability sets in. By introducing the same non-dimensional variables as the first case, we obtain the same equation (4.2). We note that the time scale $ReU/L = L^2/v$ is independent of the velocity scale U. We solve (4.2) in the domain $-\frac{1}{2} \leqslant x \leqslant \frac{1}{2}, -\frac{1}{2} \leqslant y \leqslant \frac{1}{2}$. We try a separable solution of the form

$$\omega = \sum_{\lambda} C_\lambda \omega_\lambda(x, y) \exp(-\lambda^2 t/Re). \tag{4.3}$$

Substituting into (4.2), we obtain a Helmholtz equation for ω,

$$\nabla^2 \omega_\lambda + \lambda^2 \omega_\lambda = 0. \tag{4.4}$$

Dropping the subscript λ and using $\omega = -\nabla^2 \psi$, we get

$$\nabla^4 \psi + \lambda^2 \nabla^2 \psi = 0. \tag{4.5}$$

The boundary condition is impermeable and non-slip walls. We set $\psi = 0$, $\partial \psi/\partial n = 0$ on the walls. We recall that the problem we solved for inviscid steady flows in §3 was

$$\nabla^2 \psi + \lambda^2 \psi = 0, \tag{4.6}$$

with a given fuctional form of ψ along the walls (source–sink forcing) and no restriction on $\partial \psi/\partial n$ (free-slip walls). The details of the solution procedure are omitted here. There are non-trivial solutions only for special values of λ^2 (eigenvalues). This is different from the inviscid problem for which the value of λ^2 is arbitrary. The streamfunction contours and the ψ–ω relations are shown in figure 12 for the three lowest eigenmodes with the symmetry $\psi(x, y) = \psi(-x, y) = \psi(x, -y)$ and the lowest eigenmode with the symmetry $\psi(x, y) = \psi(-x, y) = -\psi(x, y)$. The streamfunctions of the former symmetry eigenmodes are similar to the three steady patterns observed and the inviscid eigenmodes calculated in §3. The eigenvalues are larger than the corresponding inviscid eigenmodes. The ψ–ω relations are almost linear and the slope is approximately λ^2. For short, we call these eigenmodes Stokes modes. For a flow consisting of a single eigenmode, the kinetic energy can be approximated as

$$E = \frac{1}{2}\rho \iint_D |\boldsymbol{\nabla}\psi|^2 \, \mathrm{d}x \, \mathrm{d}y$$

$$= \frac{1}{2}\rho\lambda^2 \iint_D \psi^2 \, \mathrm{d}x \, \mathrm{d}y$$

$$\propto \exp\left(-2\lambda^2 \frac{v}{L^2} t_*\right). \tag{4.7}$$

We define the decay rate $\alpha = 2\lambda^2 v/L^2$.

In order to estimate the relative magnitude of the viscous force in the forced flow, we measured the transition to the decaying eigenmodes after the forcing is stopped. Four initial conditions are chosen: (*a*) the single-vortex pattern by
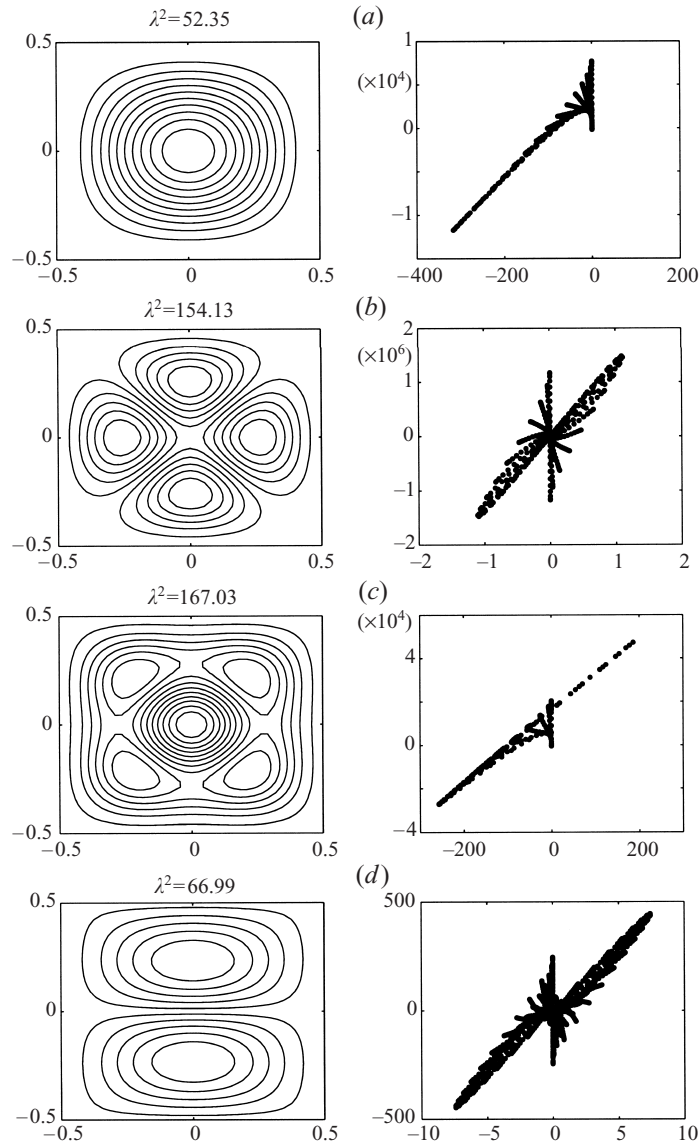
I. Kanda and P. F. Linden

FIGURE 12. Streamfunction contours and ψ–ω relations of the Stokes modes.
Each mode is a solution to $\nabla^4\psi + \lambda^2\nabla^2\psi = 0$.

the corner-source configuration with $V = 1.9\,\mathrm{cm\,s^{-1}}$, (*b*) the four-vortex pattern by the *a-a-a* configuration with $V = 1.9\,\mathrm{cm\,s^{-1}}$, (*c*) the five-vortex pattern by the side-source configuration with $V = 1.9$ and $2.1\,\mathrm{cm\,s^{-1}}$, (*d*) the irregular pattern by the side-source configuration with $V = 1.9\,\mathrm{cm\,s^{-1}}$.

Figure 13(*a*) shows the velocity and the streamfunction mappings and the ψ–ω relations by the corner-source configuration with $V = 1.9\,\mathrm{cm\,s^{-1}}$. The initially near-square vortex becomes circular as the decay progresses. The two lines in the ψ–ω plots are $\omega = 2\pi^2\psi = 19.74\psi$ for the lowest inviscid homogeneous eigenmode $\cos\pi x \cos\pi y$, and $\omega = 52.35\psi$ for the lowest Stokes mode. By 80 min, the data points lie along $\omega = 52.35\psi$. The deviation from the straight line near the left-hand end is quite
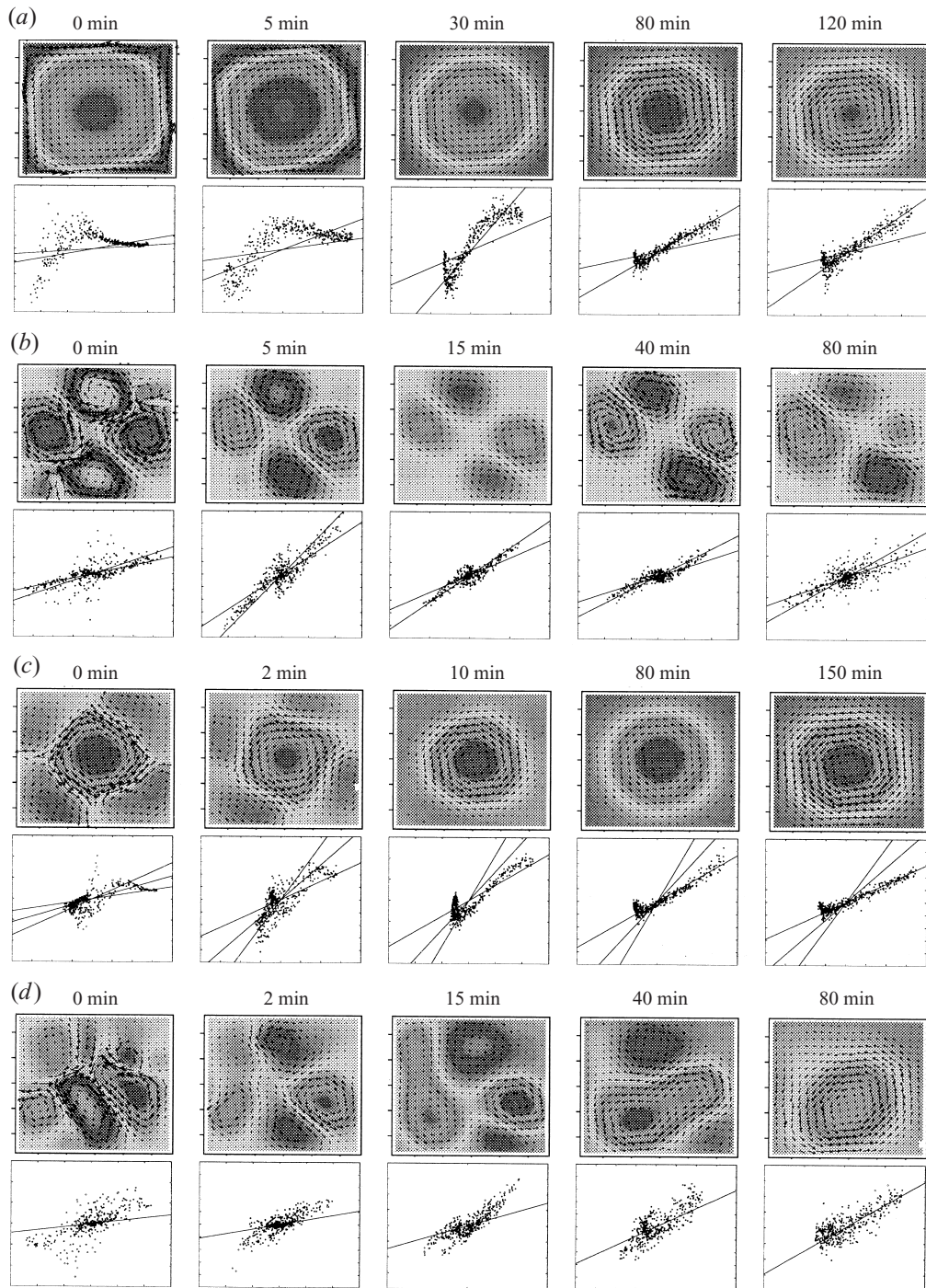
FIGURE 13. Streamfunction contours and ψ–ω relations during decay from four initial conditions. The scales are omitted and different for each figure: (*a*) corner-source, $V = 1.9\,\mathrm{cm\,s^{-1}}$; (*b*) *a-a-a*, $V = 1.9\,\mathrm{cm\,s^{-1}}$; (*c*) side-source, steady, $V = 1.9\,\mathrm{cm\,s^{-1}}$; (*d*) side-source, irregular, $V = 1.9\,\mathrm{cm\,s^{-1}}$. The lines in the ψ–ω plots are (*a*) $\omega = 2\pi^2\psi, 52.35\psi$, (*b*) $\omega = 10\pi^2\psi, 154.13\psi$, (*c*) $\omega = 52.35\psi, 10\pi^2\psi, 167.03\psi$, (*d*) $\omega = 52.35\psi$.

similar to the calculation result in figure 12(a) with the right and the left reversed. The typical velocity at 80 min is 0.2 mm s^{-1} and hence $Re \sim 120$. The validity of the Stokes flow calculation for this large value of Re relies on the fact that the velocity field is almost a circular shear flow. If the streamlines are not circular, as they are at the initial time of the decay, the inertia is not negligible.

Figure 13(b) shows the velocity and the streamfunction mappings and the ψ–ω relations by the *a-a-a* configuration with $V = 1.9$ cm s^{-1}. The initially four-fold-symmetric vortices separate into two dipoles. At 80 min, there is significant asymmetry within the dipoles and it is expected that the flow pattern ends up as a single dominant vortex. The two lines in the ψ–ω plots are $\omega = 10\pi^2\psi = 98.70\psi$ for the inviscid homogeneous eigenmode $\cos 3\pi x \cos \pi y - \cos \pi x \cos 3\pi y$, and $\omega = 154.13\psi$ for the second lowest even-symmetry Stokes mode. Initially, the data points are closer to $\omega = 98.70\psi$, but by 15 min they lie along $\omega = 154.13\psi$. The deviation from the straight line is quite similar to the calculation result in figure 12(b). The large scatter at 80 min is due to the larger relative error. The Reynolds number at 15 min is about 240.

Figure 13(c) shows the velocity and the streamfunction mappings and the ψ–ω relations for the five-vortex pattern by the side-source configuration with $V = 1.9$ cm s^{-1}. The result for $V = 2.1$ cm s^{-1} is similar and not shown here. As mentioned in §2, there is only a probability of about 20% of obtaining the steady five-vortex pattern. When the steady pattern was not achieved, the decay measurement was nonetheless included as an irregular initial pattern. If we can apply the Stokes mode calculation result, though the Reynolds number is considerably larger than unity, the decay rate of the five-vortex pattern should be almost the same as the four-vortex pattern. Hence we expected the five-vortex pattern to persist for about an hour and that one of the vortices would survive due to asymmetry. However, after 10 min the central vortex overshadowed the outer four vortices and the flow turned into a single-vortex pattern. We see at 2 min that the outer four vortices are skewed in the direction of the central vortex rotation. The elliptically deformed vortices decay with increased shear, leading to the quick domination of the central vortex. The lines in the ψ–ω plots are $\omega = 10\pi^2\psi = 98.70\psi$ for the inviscid homogeneous eigenmode $\cos 3\pi x \cos \pi y + \cos \pi x \cos 3\pi y$, $\omega = 52.35\psi$ for the lowest Stokes mode, and $\omega = 167.03\psi$ for the third lowest even-symmetry Stokes mode. The data points get closer to $\omega = 52.35\psi$ as the central vortex occupies the domain. Re is about 100 at 80 min.

Figure 13(d) shows the velocity and the streamfunction mappings and the ψ–ω relations for one of the two runs of the irregular pattern by the side-source configuration with $V = 1.9$ cm s^{-1}. The vortices merge into three by 15 min. After 15 min, the two like-sign vortices merge into a larger vortex and by 80 min occupy the whole domain. In the other case, the vortices merge into a dipole by 20 min and one of the pair dominates the other and occupies the domain by 100 min. The line in the ψ–ω plots is $\omega = 52.35\psi$ for the lowest Stokes mode. We see the gradual approach to this line as the number of vortices decreases. For both the cases, $Re \sim 20$ at 80 min.

We next compare the observed decay rates with the Stokes mode calculation result. The kinetic energy is represented by the mean-square velocity magnitude in the region $-225.0 \leqslant x \leqslant 218.2$ mm, $-221.0 \leqslant y \leqslant 217.0$ mm. The peripheral grid points shown in the previous figures are excluded since they are close to the source–sink forcing and the values of the velocity are often erroneous due to the three-dimensionality of the flow. Figure 14 shows the kinetic energy against time. The inserted lines have the slopes corresponding to the decaying Stokes modes. For the corner-source and the
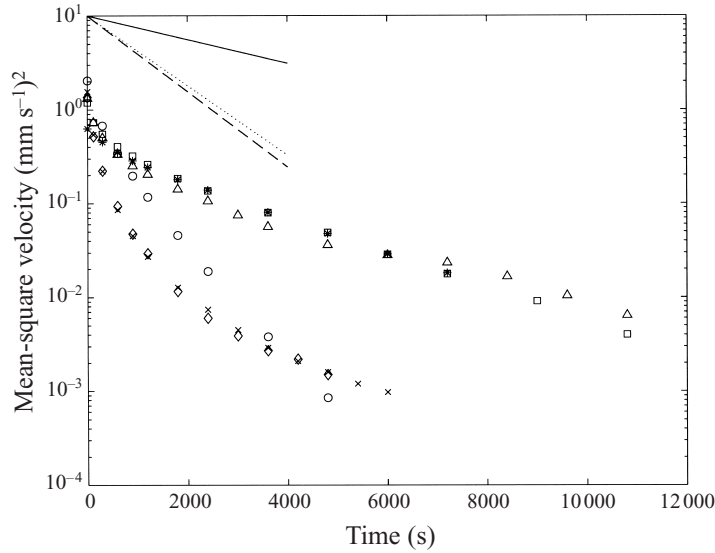
FIGURE 14. Kinetic energy decay behaviour. $*$, corner-source, $V = 1.9\,\mathrm{cm\,s^{-1}}$; $\bigcirc$, *a-a-a*, $V = 1.9\,\mathrm{cm\,s^{-1}}$; $\square$, side-source, steady, $V = 1.9\,\mathrm{cm\,s^{-1}}$; $\triangle$, side-source, steady, $V = 2.1\,\mathrm{cm\,s^{-1}}$; $\times\lozenge$, side-source, irregular, $V = 1.9\,\mathrm{cm\,s^{-1}}$. The lines from the top-right corner represent the decay rate of the Stokes modes in figure 12; (*a*) solid line, (*b*) dotted line, (*c*) broken line.

Experiment	$V\,(\mathrm{cm\,s^{-1}})$	Calculation period (s)	$\alpha\,(\mathrm{s^{-1}})$
Corner-source	1.9	2400–7200	4.25×10^{-4}
Side-source			
Irregular	1.9	4200–6000	4.31×10^{-4}
	1.9	3000–4800	5.12×10^{-4}
Steady	2.1	1800–3600	5.17×10^{-4}
		4800–7200	1.82×10^{-4}
		8400–10800	3.97×10^{-4}
	1.9	2400–10800	4.15×10^{-4}
a-a-a	1.9	1800–4800	1.33×10^{-3}

TABLE 1. Decay rate α in the linear part of figure 14.

a-a-a configurations, the kinetic energy decays exponentially except at early times. The decay rate of the latter is considerably larger than the former. For the side-source configuration, the initial decay rate is comparable to that of the *a-a-a* configuration, but as the flow field is occupied by a single vortex, the decay rate becomes almost the same as that of the corner-source configuration.

We write the kinetic energy as proportional to $\exp(-\alpha t_*)$, and the values of α calculated by the least-square method in the final linear part of the decay plot are shown in table 1. The values of α for the lowest and the second lowest even-symmetry Stokes modes are 2.91×10^{-4} and 8.56×10^{-4}, respectively. The experimental values are larger because of the dissipation due to the vertical shear. We do not have a satisfactory explanation for the slow decay at 4800–7200 s of the side-source, steady experiment at $2.1\,\mathrm{cm\,s^{-1}}$. One possible explanation is that the velocity field changed

from the five-vortex pattern to the single-vortex pattern across this time range and the slow decay is due to the smaller horizontal shear during the expansion of the central vortex. However, we do not see any significant change in the shape or slope of the ψ–ω plots during this period. Hence, this explanation should be discarded. If we neglect this anomaly, the decay rate for the single-vortex pattern is $3.97 \sim 5.12 \times 10^{-4}$ and that for the four-vortex pattern is 1.33×10^{-3}. Suppose we can separate the dissipation into horizontal and vertical contributions, then the contribution from the vertical shear is $1.06 \sim 2.21 \times 10^{-4}$ for the single-vortex pattern and 4.7×10^{-4} for the four-vortex pattern. This large difference shows that we need a three-dimensional analysis to evaluate the decay rate quantitatively.

We have seen that the transition from a forced flow to a Stokes mode is completed at quite large values of Re. This is realized by rearranging the velocity field into an almost inertialess one, rather than by the reduction of the velocity magnitude. The change in the appearance of the velocity field is slight, just as the modification of the forced flow by the vorticity diffusion was small.

5. Discussion

We first summarize our results and then restate three problems.

In the horizontal flow produced by the source–sink forcing method, we revealed the sensitivity of the flow patterns to the forcing geometry. For particular source–sink configurations, the flow evolves into steady patterns which resemble the eigenmodes of the Helmholtz equation in a square domain. The thresholds between patterns are sensitive to small errors in the experimental setup. We showed that such eigenmodes are possible solutions for the given boundary conditions including small deviations from the intended symmetry. However, there is significant discrepancy in the stream-function *vs.* vorticity relations between the analytical solutions and the observed flows. We attribute it to the viscous diffusion of vorticity from the source flows. In order to see how much the flow field is changed when the viscous force dominates over the inertia force, we studied the transition to a low-Re decaying flow which has a narrower spectrum of solutions (Stokes modes). The Stokes modes are quite similar in appearance to the steady patterns we observed in the forced flow. The decay experiment revealed transitions to Stokes modes at unexpectedly large Re.

The first problem is the reproducibility. As we have seen, the reproducibility is poorer for steady patterns resembling higher eigenmodes. We can explain this from two viewpoints. First, if we consider the interaction of laminar source flows, a steady pattern requires balance among impinging source flows. Since a higher mode has more impingement points, it would require more accurate symmetry for steadiness. Second, if we neglect the individual source flow and employ the idea of §3, i.e. an eigenmode is somehow selected for the given forcing, then the controlling parameter is the eigenvalue λ^2. Since λ^2 represents the kinetic energy of the horizontal motion, the eigenmodes with the same value of λ^2 are equivalent. For the Helmholtz equation in a square domain, the degeneracy of eigenmodes increases with λ^2. Hence, for higher modes, the pattern can change among equivalent eigenmodes without significant change of energy. The favourable pattern, of course, depends on the symmetry of the source–sink configuration, but the fluctuation about it becomes easier as λ^2 increases. This viewpoint, however, leaves the selection of λ^2 an open question.

The next problem is whether the approach of §3 is appropriate or not. We first derived possible solutions for arbitrary boundary conditions and explained the dis-crepancy as the effect of viscosity. However, this is an approach suitable for many

source–sink pairs for which the resultant flow pattern is only weakly affected by the source–sink configuration. An alternative approach is to focus on individual source flows and analyse the interaction among them. This approach is appropriate when there are a few source–sink pairs and the resultant flow pattern is determined by the source–sink configuration. As a one-pair case, A. L. Kurapov (personal communication) used a similar source–sink system in a rectangular domain and observed asymmetric or oscillatory patterns. Related works report symmetry-breaking bifurcations of the flow into a channel through a sudden expansion (see for example Sobey 1985; Sobey & Drazin 1986). The rich bifurcation behaviour of these one-pair cases indicates much more complicated behaviour for many-pair cases. The sensitivity to small errors of our four- or eight-pair cases represents this character. In order to evaluate the complexity of the dynamics of four- or eight-pair cases, further study with one- or two-pair forcing is in progress. It is also of interest whether the sensitivity to the forcing configuration is lost for source–sink forcing with more pairs. Then two-dimensional turbulence theories may be applicable to the central region of irregular jet interaction.

Finally, we discuss the transition to the Stokes modes at relatively large Re. As we mentioned in §4, such a transition is possible if the inertia term is small, owing to the flow field structure. The nearly circular streamfunction contours suggest this is the case. Also, even in the forced state, the stability of the observed steady patterns which are not strictly steady in our convention suggests that the relative magnitude of the inertia force can be easily diminished by deformation. In order to analyse the stability of the flow patterns, computational solution of the full Navier–Stokes equation may be necessary because the ratio of the inertia to the viscous force can vary spatially from much less than unity to the nominal Re.

REFERENCES

BATCHELOR, G. K. 1969 Computation of the energy spectrum in homogeneous two-dimensional turbulence. *Phys. Fluids Suppl.* **II**, 233–239.

BOUBNOV, B. M., DALZIEL, S. B. & LINDEN, P. F. 1994 Source-sink turbulence in a stratified fluid. *J. Fluid Mech.* **261**, 273–303 (referred to herein as BDL).

CHAVANIS, P. H. & SOMMERIA, J. 1996 Classification of self-organized vortices in two-dimensional turbulence: the case of a bounded domain. *J. Fluid Mech.* **314**, 267–297.

DALZIEL, S. B. 1993 Rayleigh–Taylor instability: experiments with image analysis. *Dyn. Atmos. Oceans* **20**, 127–153.

GOODWIN, R. T. & SCHOWALTER, W. R. 1996 Interactions of two jets in a channel: solution multiplicity and linear stability. *J. Fluid Mech.* **313**, 55–82.

KONIJNENBERG, J. A. VAN DE, FLÓR, J. B. & HEIJST, G. J. F. VAN 1998 Decaying quasi-two-dimensional viscous flow on a square domain. *Phys. Fluids* **10**, 595–606.

SOBEY, I. J. 1985 Observation of waves during oscillatory channel flow. *J. Fluid Mech.* **151**, 395–426.

SOBEY, I. J. & DRAZIN, P. G. 1986 Bifurcation of two-dimensional channel flows. *J. Fluid Mech.* **171**, 263–287.